Optimization of an high-pressure turbine vane for pressure gain combustion cycles through convolutional neural network

Energy and AI 24 (2026) 100729

Contents lists available at ScienceDirect

Energy and AI

journal homepage: www.elsevier.com/locate/egyai

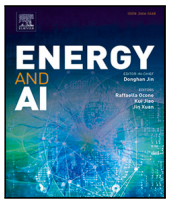

Optimization of an high-pressure turbine vane for pressure gain combustion cycles through convolutional neural network

Giovanni Labrini, Rosario Nastasi, Simone Salvadori *, Daniela Anna Misul

Turbomachinery for Energy and Propulsion (TEP) group, Politecnico di Torino, Corso Duca degli Abruzzi, 24, Torino, 10129, Italy

GRAPHICAL ABSTRACT

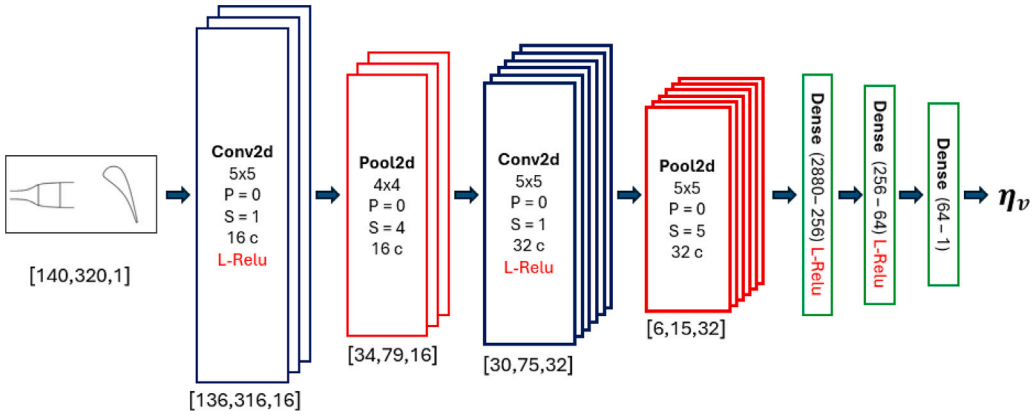

HIGHLIGHTS

- Convolutional Neural Network for turbine vane design with diffusive endwalls.
- Comparison of optimized geometries obtained using data- and image-based methods.
- Testing the optimized configurations under realistic pulsating inlet conditions.

ARTICLE INFO

Keywords:
Artificial intelligence
Machine learning
Convolutional neural networks
Computational fluid dynamics
Gas turbines
Aero-engines
Power generation
Rotating detonation combustion

ABSTRACT

Rotating Detonation Engine (RDE) represents a pioneering technology in the propulsive and energy production fields, although the coupling with transonic High-Pressure Turbine (HPT) stages is challenging. Several studies introduced the concept of diffusive endwalls in order to ingest high-subsonic flow delivered by the RDE. Machine Learning (ML) gained a prominent role in the optimization procedures because of its fast and accurate prediction, reducing the computational time respect to Computational Fluid Dynamics (CFD). The aim of this study is to optimize the blade and endwall profiles of an HPV, targeting an enhancement of aerodynamics performance. The optimization methodology is based on several algorithms using a Convolutional Neural Network (CNN) as the fitness function, which can estimate the vane performance directly from an image containing blade and endwall profiles. The Design of Experiment (DOE) is performed using Reynolds-Averaged Navier–Stokes (RANS) analysis that takes in account 18 design variables, which represent geometric features of vane profile and diffusive endwalls. The optimized profiles are then tested under pulsating boundary conditions from a Rotating Detonation Combustor (RDC) to understand which configuration can perform adequately under

* Corresponding author.
E-mail address: simone.salvadori@polito.it (S. Salvadori).

https://doi.org/10.1016/j.egyai.2026.100729
Received 6 October 2025; Received in revised form 16 December 2025; Accepted 23 March 2026
Available online 31 March 2026

extremely harsh conditions. The CNN coupled with Particle Swarm Optimization (PSO) increases the vane efficiency with respect to nominal configuration and the novel design proved to be affordable also in presence of variable inlet conditions, attenuating pressure oscillations.

Nomenclature

P_t	Total pressure
T_t	Total temperature
P	Static pressure
T	Static temperature
A	Area
u	Velocity magnitude
D_R	Damping coefficient
$\hat{R}$	Reduced range
R^2	Coefficient of determination
Ma	Mach number
t	Time
$\dot{m}$	Mass flow rate
C	Vane chord

Acronims

RDE	Rotating Detonation Engine
RDC	Rotating Detonation Combustor
CNN	Convolutional Neural Network
DNN	Deep Neural Network
GA	Genetic Algorithm
PSO	Particle Swarm Optimization
DOE	Design of Experiment
GTs	Gas Turbine
ML	Machine Learning
PGC	Pressure Gain Combustion
HPT	High-Pressure Turbine
RANS	Reynolds-Averaged Navier–Stokes
URANS	Unsteady RANS
PV	Passage Vortex
URANS	Unsteady RANS

Greek letters

η_v	Vane efficiency
α	Flow angle
γ	Heat capacity ratio
ζ_{P_t}	Total pressure loss coefficient
ζ_α	Deviation coefficient
ρ	Density

Superscripts and subscripts

MA	Mass-weighted average
AA	Area-weighted average
WA	Working average
CA	Cycle average
1	Inlet of the vane
2	Outlet of the vane

1. Introduction

Recent efforts in the context of Gas Turbines (GTs) for propulsion and power generation aim at increasing both overall efficiency and specific power to reduce the fuel consumption and pollutant emissions by using advanced numerical methods for component interaction analysis at engine scale [1].

The Rotating Detonation Engine (RDE) has proved to be one of the most promising Pressure Gain Combustion (PGC) technologies, aimed at increasing the cycle efficiency with respect to the traditional Joule–Brayton cycle [2,3]. The RDE engine implements an annular chamber (namely, the Rotating Detonation Combustor, RDC) where a detonation wave ignites the fuel and air mixture [4,5]. Despite the benefits brought by this new technology [6], some challenging aspects are present due to the harsh combustor outflow conditions, characterized by a spatial–temporal variation of stagnation pressure, stagnation temperature, and flow angle [6–8]. The High-Pressure Turbine (HPT) stage efficiency could be influenced negatively by these inlet conditions, therefore it is important to assess that the HPT efficiency deficit would not counteract the cycle efficiency improvement obtained by using the RDC.

Considering the coupling of RDC with transonic vanes, Liu et al. [9] proposed modified endwalls of the vane to keep the contraction ration below the isentropic limit, and made numerical analysis on a conventional HPT stage under uniform axial pulsation and an inlet Mach number of 0.3 and 0.6. This work has highlighted the generation of separation bubbles in the diffusive endwalls. In another work, Liu et al. [10] showed that inlet Mach number of 0.3 brings an higher stage efficiency while a Mach of 0.6 gives higher attenuation. Grasa et al. [11] proposed a multi-point optimization strategy with CFD analysis, focusing on reduction of total pressure losses and homogeneity of vane's outflow to prevent blade's forcing. Later, Gallis et al. [12] presented a parametric optimization for both the diffusive endwalls and the airfoil, implementing a passive flow control system through an array of cooling holes placed upstream the leading edge. The flow control system has proved to mitigate the oscillating inflow conditions and better guide the outflow that approach the subsequent rotor.

In recent years, Machine Learning (ML) proved to be an useful tool in the optimization process of HPT, because of the possibility to replace High-fidelity CFD simulations with ML-based surrogate models, which require less computational and time resources to explore the design space [13–16]. Du et al. [17] implemented a dual Convolutional Neural Network (CNN) to predict the performance of a turbine blade profile design. The ML is trained over RANS CFD simulations to predict the physical field distribution based on design variables and evaluate aerodynamic performance. Nastasi et al. [18] studied a parametric optimization for both the diffusive endwalls and the airfoil of a transonic vane for RDE, implementing a Deep Neural Network and Random Forest regressor as surrogate models, then a Genetic Algorithm to find the optimal configuration based on an objective function. Their optimized geometry achieved strong mitigation of the intensity of the secondary flows and higher aerodynamic efficiency increased with respect to the baseline design.

The idea of this project is to feed a Convolutional Neural Network (CNN) with images representing the endwall and the profile shape of several redesigns of an academic turbine vane by Gallis et al. [12], with the goal to evaluate the aerodynamic performance. The original stator blade and endwalls are parameterized by means of splines and a range of variability is defined for each parameter. Then a Design of Experiment (DOE) is performed exploring almost 900 configurations through the Latin Hypercube Sampling (LHS) method. The DOE configurations are evaluated with CFD RANS simulations which provided the vane efficiency, the exit flow angle and other performance parameters. The CNN is then trained on the dataset provided by the RANS simulations and returned the vane efficiency as output. The trained CNN is applied as meta-model in two different optimization algorithm: Genetic Algorithm (GA) and Particle Swarm Optimization (PSO). Both

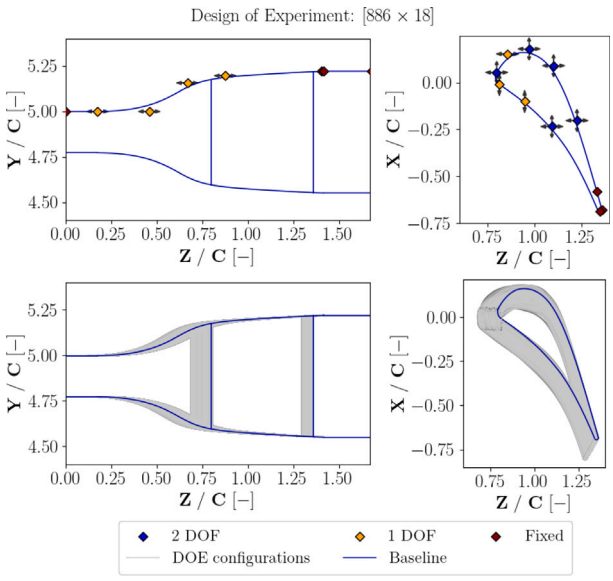

Fig. 1. DOE design variables for vane profile and endwall.

Table 1
Geometrical feature of the nominal CT3 vane.

C	75.7 [mm]
N_{Vane}	43 [–]
R_{Shaft}	369.85 [mm]
DR_{Inlet}	8.6 [mm]
DR_{Outlet}	23.25 [mm]

the optimized profiles and the one optimized by Nastasi et al. [18] are then tested with synthetic pulsating boundary conditions from a Rotating Detonation Combustor (RDC). The CNN produced extremely faster predictions of the vane efficiency respect to the traditional CFD analysis, this allowed to explore extensively the design space without generating the CAD of the geometry which implied a reduction of the global time of the optimization analysis.

2. Blade aerodynamics and parametric study

The nominal vane profile used in this study is the one already analyzed by both Gallis et al. [12] and Nastasi et al. [18], its geometrical features are reported in Table 1. It presents diffusive endwalls, which consist of an enlargement of the inlet section, and a redesigned vane to allow for a higher inlet Mach number value of ≈0.6 with respect to the original working condition of ≈0.2 that was studied by Sieverding et al. [19] Denos et al. [20,21], and Paniagua et al. [22].

In Fig. 1 the blade and endwalls parameterization, originally proposed by Liu et al. [23] and Gallis et al. [12], is presented. It consists of:

- 7 spline control points for the endwalls, which are considered symmetric respect to x-axis. 4 of them can move along the z-axis while the others are fixed.
- 11 spline control points for the blade profile, 7 for the suction side and 5 for the pressure side. 5 of them has two degrees of freedom, 3 can move on one direction and the remaining are fixed.

The blade stagger angle is also considered variable, this brings to 18 design variable that are included in the Design of Experiment (DOE) phase.

The Design of Experiment is conducted adopting the Latin Hypercube Sampling approach, which divide the design space in evenly spaced sub-intervals and randomly select design point from these sub-intervals. The design space selected consists in 900 sampling points of which 886 completed the generation, mesh and CFD simulation process.

2.1. Evaluation of the vane

The vane performance are evaluated using several performance parameters. The vane efficiency provides a measure of the total pressure P_t losses between the inlet (1) and the outlet (2) of the vane, as expressed in Eq. (1):

$$\eta_v = \frac{1 - \left(\frac{P_2}{P_{t,2}}\right)^{\frac{\gamma-1}{\gamma}}}{1 - \left(\frac{P_2}{P_{t,1}}\right)^{\frac{\gamma-1}{\gamma}}} \tag{1}$$

The vane efficiency is the only output of the optimization strategy, then for this reason the deviation coefficient of the exit flow angle α_2 respect to the metal angle $\alpha_{2,m}$, is computed to evaluate the vane configurations as in Eq. (2):

$$\zeta_\alpha = 1 - \frac{\alpha_2}{\alpha_{2,m}} \tag{2}$$

2.2. Evaluation of the pulsating boundary condition

The URANS analysis requires different quantities to compute due to the pulsating nature of the flow. It is also important to assess that the quantities of interest are computed after the initial transitory phase, in other word that the periodicity is established.

The cross-correlation is performed between two sequential cycles of the periodic boundary condition for each property monitored in time (see Eq. (3)). The maximum, minimum and average values of cross-correlation for zero lag in various locations can be computed. The cycle periodicity can be established as the cross-correlation value is close to unity.

$$\hat{C}_{12}(\tau) = \frac{1}{t_0}\int_0^{t_0} \phi_1(t)\ \phi_2(t+\tau)\ dt \tag{3}$$

Calculating instantaneously the vane efficiency could lead to time moments when the inlet total pressure is lower than the outlet one, bringing a value that exceeds the unity. To avoid this problem, the cycle average of the flow are applied, according what is suggested by Cumpsty et al. [24]. According to this approach, the extensive properties and total temperature can be mass-weighted averaged, the averaging equation for a generic property ϕ is defined by Eq. (4).

$$\overline{(\phi)}^{MA} = \frac{\int_0^\tau \phi^{MA} \cdot \int_A \rho u\ dA\ dt}{\int_0^\tau \int_A \rho u\ dA\ dt} \tag{4}$$

Total pressure follows a different averaging process for turbomachinery applications, as it stated in several literature works [25–27] (Eq. (5)).

$$\overline{P}_t^{WA} = \left[\frac{\int_0^\tau \int_A \rho u T_t\ dA\ dt}{\int_0^\tau \int_A \rho u [T_t/P_t^{\frac{\gamma-1}{\gamma}}]\ dA\ dt}\right]^{\frac{\gamma-1}{\gamma}} \tag{5}$$

Static outlet pressure oscillates in time as well. In Gallis et al. [12] the time average value takes in account the area-average value following Eq. (6):

$$\overline{P}^{AA} = \frac{1}{\tau A}\int_0^\tau \int_A P\ dA\ dt \tag{6}$$

The properties time-averaged quantities are defined, so the performance quantities can be rewritten to incorporate the oscillating behavior in time. The vane efficiency follows the definition given by Young et al. [28] (Eq. (7)):

$$(\overline{\eta_v})^{CA} = \frac{1 - \left(\frac{T_2^{MA}}{T_{t,2}^{MA}}\right)}{1 - \left(\frac{P_2^{AA}}{P_{t1}^{WA}}\right)^{\frac{\gamma-1}{\gamma}}} \tag{7}$$

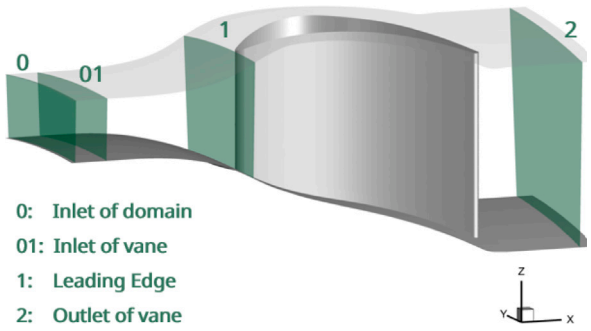

Fig. 2. CT3 sampling location for cross-correlation and damping coefficient.

Table 2
Boundary conditions for DOE RANS analysis.

BC type	Value
Inlet	$P_t = 161\,600$ [Pa] | $T_t = 440$ [K] | $\alpha = 0°$
Outlet	$P = 83\,289$ [Pa]
Periodic	Rotational 8.37°
Wall	No-slip (Adiabatic)

Also, the deviation coefficient can be formulated according to the cycle averaging technique (Eq. (8)):

$$(\overline{\zeta_\alpha})^{CA} = 1 - \frac{(\overline{\alpha_2})^{MA}}{\alpha_{2,m}} \tag{8}$$

The vane can be evaluated in terms of pressure losses, according to Eq. (9):

$$(\overline{\zeta_{Pt}})^{CA} = \frac{P_{t2}^{MA} - P_{t1}^{MA}}{P_{t1}^{MA}} \tag{9}$$

The damping coefficient (Eq. (10)) expresses how the vane responds to the oscillating inflow conditions such as the total pressure. It is usually computed for two consecutive locations as function of the reduced range that is defined in Eq. (11):

$$D_{R,Pt} = \frac{\hat{R}_1 - \hat{R}_2}{\hat{R}_1} \tag{10}$$

$$\hat{R} = \frac{Max(P_t^{MA}) - Min(P_t^{MA})}{\frac{1}{\tau}\int_0^\tau P_t^{MA}\, dt} \tag{11}$$

3. Numerical methodology

3.1. Design of experiment

In the current study the commercial software *ANSYS CFX™ 2022 R1* is used to generate the data to train the Convolutional Neural Network, which is based on steady RANS simulations. The k-ω SST turbulence model is adopted for this study, applying a coupled pressure-based solver with "high resolution" scheme for advection and turbulence discretization. The mesh consisted in a hybrid tetrahedral–prismatic mesh of about 2 millions of elements, with 20 inflation layers to achieve a $y^+ \leq 1$ in the wall region. More details about the mesh and the Grid Convergence Index (GCI) are reported in the work of Nastasi et al. [18].

In Fig. 3 and Table 2 the boundary conditions imposed for the DOE RANS simulations are listed.

3.2. Unsteady analysis

The unsteady RANS CFD analysis is carried out employing the commercial software *ANSYS Fluent™ 2023 R2*. The boundary conditions in the inlet section are assumed to change in time, aiming to reproduce the behavior of a flow coming from the outlet of a transition duct coupled

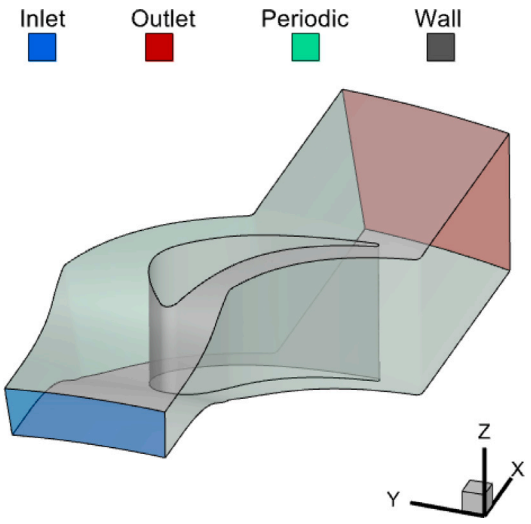

Fig. 3. Nominal configuration and boundary conditions.

Table 3
Boundary conditions URANS analysis.

BC type	Value
Inlet	$P_t = f(t)$ [Pa] | $T_t = f(t)$ [K] | $\alpha = f(t)$
Outlet	$P = 83\,289$ [Pa]
Periodic	Rotational 8.37°
Wall	No-slip (Adiabatic)

with an RDE. In particular, this analysis focuses on a variation of inlet total pressure, inlet total temperature and flow angle in circumferential direction, as it is shown in Fig. 5 and Table 3.

A number of hypotheses have been done to finalize the morphology of the signals. First, it is assumed that for the current working conditions the RDC generates a single traveling mode at a frequency (5000 Hz) that is one order of magnitude higher than the typical rotational speed of a turbine blade (≈500 Hz). Therefore, a single shock is considered to mimic the discontinuity in the signals at the vane inlet. Moreover, instead of simulating a traveling wave a pulsating condition is applied in time to analyze the performance of the newly-designed vane. The latter simplification is acceptable as the main topic of this work is the capability of the CNN model to accurately design enabling technologies for RDEs. Furthermore, it is assumed that between the RDC and the vane an appropriately designed transition duct allowed for generating the optimal boundary conditions for a turbine stage with a inlet Mach number of ≈0.6 and with reduced total pressure fluctuations. In fact, there is still some debate in literature about the shape of the duct that should follow an RDC, either a sudden expansion or a diffuser [29,30] or an ejector [31], but it is not of interest here to study this specific component. In this activity the final morphology shown here is the same one adopted in the work of Gallis et al. [12] (see Fig. 4).

The k-ω SST turbulence model is adopted for this study, applying a density-based solver with second order upwind flux scheme.

The mesh is composed of $\approx 2.1 \cdot 10^6$ hybrid tetrahedral and prismatic elements. The mesh is identical to the one used in the DOE, except for a slight modification in the CAD, that exhibits an artificial plenum placed downstream the trailing edge of the blade. As it is possible to notice in Fig. 6, the artificial plenum presents a coarser mesh respect to the vane region, in order to dissipate any phenomenon that can occur as the trailing edge of the vane, that may bring non-physical results. To keep low the number of elements, slip wall boundary condition is applied and no inflation layer are used in this region of the domain.

The size of the mesh is selected after a process of GCI, that took in account inlet mass-flow rate, the inlet mass-weighted averaged Mach

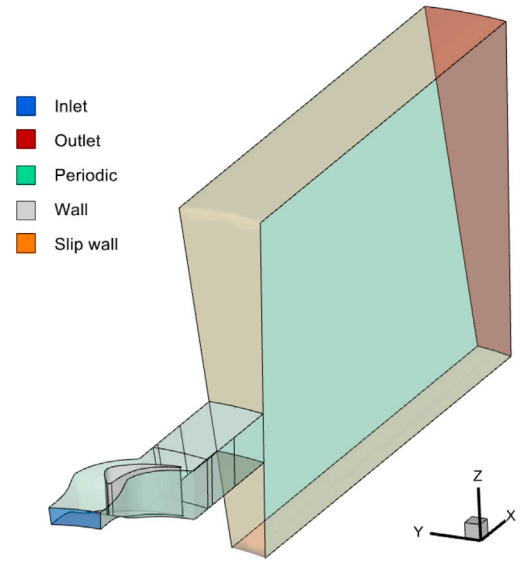

Fig. 4. URANS boundary conditions.

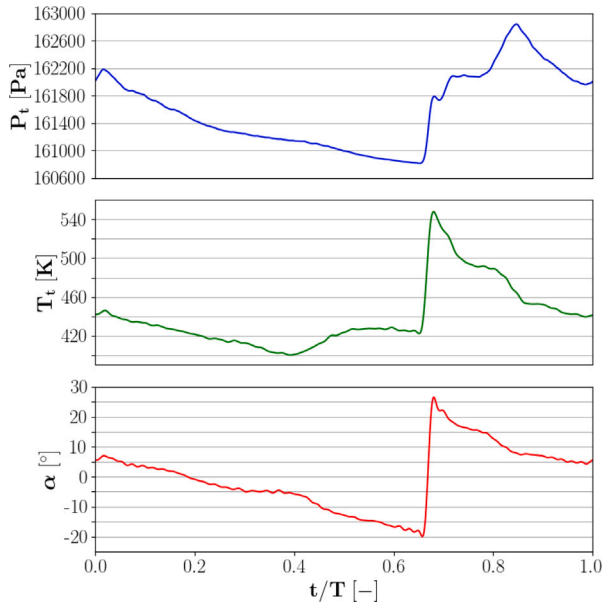

Fig. 5. RDC synthetic inlet boundary conditions for URANS analysis: total pressure, yaw angle, and total temperature.

number, and the mass-weighted averaged total pressure at the outlet of the vane under three different levels of size. The refinement ratio is 1.14 between the coarse-medium and the medium-fine, for each property the GCI decreases and the asymptotic ranges is closer to the unit as it is stated in Table 4. Thus the results obtained can be considered grid independent.

4. Machine learning and optimization strategies

4.1. Convolutional neural network

Convolutional Neural Networks are particular types of Machine Learning models that operates with images or grid-like topology. An image can be sampled in different pixels, where each pixel assumes specific values according to it is color. This implies that an image can be represented as a tensor that has dimension $w \times h \times c$, where w is the

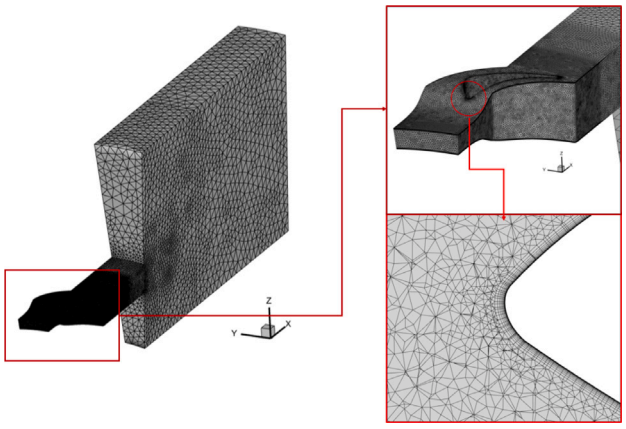

Fig. 6. CT3 URANS mesh.

Table 4
Grid Convergence Index for unsteady calculation.

	GCI (C-M)	GCI (M-F)	Asymptotic range
$\dot{m}_1$	0.0273%	0.0014%	1.043
Ma_1	0.0676%	0.0053%	1.04
$P_{t,2}$	0.1466%	0.0299%	1.015

number of pixels that fill the width of the image, h the pixels along the height and c the number of channel colors that are used in the image. Considering a black and white image, this value is equal to 1, which implies that the tensor becomes a matrix.

This type of Neural Network is characterized by a particular type of layer called convolutional layer, because of the operation it performs. Considering a matrix of learning parameters called kernel H and a portion of the tensor, the convolutional operation can be defined as in Eq. (12) [32]:

$$z_{ij} = \sum_{a=1}^{l}\sum_{b=1}^{l} H_{ab} x_{(i+a),(j+b)} \tag{12}$$

This operation changes the dimensions of the resultants tensor according to Eq. (13), where n is the input dimension, l the kernel size, p the padding size and s the stride size:

$$W_z = \frac{n - l + 2p}{s} + 1 \tag{13}$$

Padding is used when the user wants to preserve the information on the borders of the image and consists in adding some zeros, surrounding the original matrix. The stride is related to how many steps the filter travels each time it moves along the matrix.

Pooling layer is another type of layers commonly used in CNN architectures that aims at reducing the information of the input tensor to obtain the desired result. A typical CNN architecture is composed by convolutional and pooling layers that reduce the input size on the image and identify key information with a number of filters called channels, then the final tensor is flattened in a fully connected layer which is connected to other simple dense layers.

A traditional dense layer takes as input a one-dimensional array and multiplies for a matrix of weights w_i and sums the result to an array of bias values b_i (see Eq. (14)).

$$z_i = \sum_{i}^{N} (w_i \cdot x_i + b_i) \tag{14}$$

The difference between this solution and a simple linear regression is the use of the activation functions, that add non-linearity to the model and allow for capturing the relationship between input and output. In a regression context, Rectified Linear Unit (ReLU) and its

modified versions are usually implemented. The Leaky ReLU activation function used in this work can be expressed as it stated in Eq. (15).

$$f_{L-ReLU}(x) = max(ax, x) = \begin{cases} x & \text{if } x \geq 0 \\ ax & \text{if } x < 0 \end{cases} \tag{15}$$

The values of weights, biases and also kernel elements need to be adjusted to the value that represent the correct outputs from the given input. This process is named "training" and it is based on the computation of a loss function L between the output y and the expected target $\hat{y}$.

$$L(y, \hat{y}) = MSE(y, \hat{y}) = \frac{1}{n}\sum_{i=1}^{n}(y_i - \hat{y}_i)^2 \tag{16}$$

The training phase is done on a certain percentage of the dataset while the remaining part forms the validation dataset, which is used to understand if the model predicts correctly also the unseen data or only the data on which it was trained. To avoid the latter situation, called "overfitting", dropout, mini-batches, and L2 regularization are applied. The dropout consists in turning off a certain percentage of neurons during the training phase, thus helping the model to be more general. The mini-batches approach consists in computing the loss and the gradient for a certain number of subdivisions of the entire training dataset. Finally the L2 normalization consists in adding a term to the loss function which is the squared norm of the weights in order to penalizing large weights in the model.

$$\tilde{L}(y, \hat{y}) = L(y, \hat{y}) + \lambda \|w\|_2^2 \tag{17}$$

The ADAM optimizer, introduced by Kingma [33], is an algorithm for first-order gradient-based optimization of stochastic objective functions, based on adaptive estimates of lower-order moments, that is implemented into the training phases to update the value of weight and biases.

4.2. Genetic Algorithm

The Genetic Algorithm (GA), developed by Holland et al. [34], is part of the family of the nature-inspired optimization algorithms and aims at finding the best possible optimum relying on a single objective fitness function. GA encodes the design variables into a string that represents the chromosomes and generates a population of solution that own different chromosomes. A new population of better individuals is generated starting from genes of the previous population, applying the following mechanisms:

- Crossover: two or more chromosomes (parents) are split in several parts to produce a new individuals (prole) that share part of the sequences of the parents.
- Mutation: spontaneous and random modification of one or more genes in the new generation of individuals.

The parents for the new generation are selected by using a fitness function that gives a score to every individual. The fitness function can be either a particular metric defined in the post-processing of a CFD analysis either a trained surrogate model, such as Neural Networks.

4.3. Particle Swarm Optimization

Particle Swarm Optimization, developed by Kennedy and Eberhart [35], is based on swarm behavior in nature, such as fish and bird schooling. The PSO algorithm searches the space of an objective function by adjusting the trajectories of the particles; each particle is influenced by the position of the current best of all the swarm (global best) g^* and its own best location x_i^* in history, while at the same time it has a tendency to move randomly and update the locations when it finds a new better solutions. The goal is to find the global best among all the current best solutions until there is no improvement in the objective or after a certain number of iterations. The solution of a given position is evaluated through a fitness function such as in Genetic Algorithm.

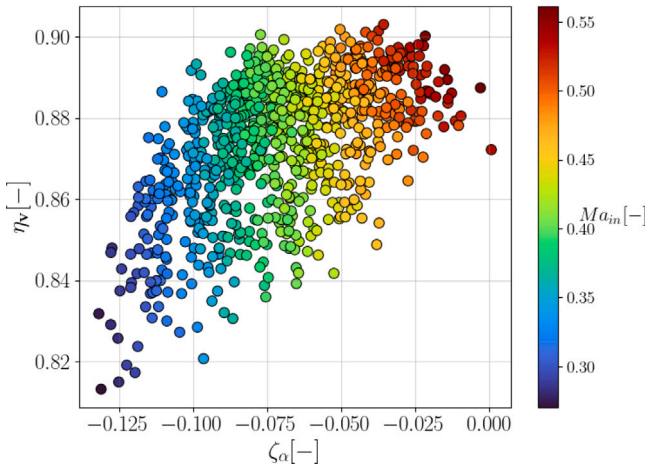

Fig. 7. Scatter plot representing of the DOE samples, obtained through RANS CFD simulations.

During the optimization process, a velocity function is computed to update the position of every particle and allow the exploration of the design space. The velocity for each particle i at next iteration $t + 1$ is defined in Eq. (18) [36]:

$$v_i(t+1) = \theta(t+1) \cdot v_i(t) + \alpha \cdot r_1 \cdot [g^* - x_i^t] + \beta \cdot r_2 \cdot [x_i^* - x_i^t] \tag{18}$$

In Eq. (18), α and β are called respectively social and cognitive coefficient and allow to decide whether to give more importance to the global best solution or to the best solution of the given particle; r_1 and r_2 are random numbers between 0 and 1; θ is the inertia weight which is linked to the velocity at the previous iteration step. Finally, the position of each particle is updated according to Eq. (19):

$$x_i(t+1) = x_i(t) + v_i(t+1) \tag{19}$$

5. Results

5.1. Design of experiment steady analysis

The DOE configurations are analyzed through RANS CFD analysis on a 48 cores CPU, that required approximately 73 h to run the 886 configurations. In Fig. 7, the results of the RANS analysis are shown in terms of vane efficiency, deviation coefficient and inlet Mach number. All the design points are subjected to same boundary conditions, which are total pressure and temperature, but each sample has a throat area that leads to a different inlet Mach number.

Results show that the geometries with a lower inlet Mach number present also a lower value for the vane efficiency and a higher deviation coefficient. The best cases of the DOE presents a stator efficiency above 0.9 and an inlet Mach number higher than 0.55, which is close to the target identified in literature [9].

5.2. Convolutional Neural Network training

The CNN architecture, built through *PyTorch* python library, consists in 2 Conv2d layers, 2 Pool2d layers and 3 Dense layers. A conceptual scheme of the architecture of the CNN is reported in Fig. 8 and Table 5. The black and white image of endwalls and blade profile is transformed into a 2D array, then the convolutional layers extract information by the kernels that expand the dimension of the array, adding the 3rd dimension. The pooling layers reduce the array dimensions and a flattening operation is applied after the second pooling layer, which

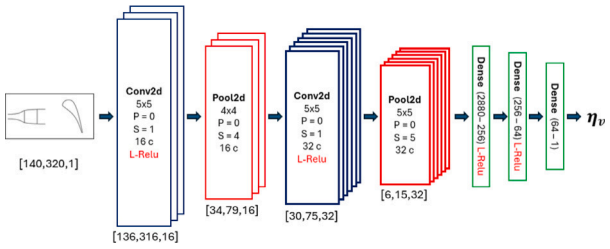

Fig. 8. CNN scheme.

Table 5
Convolutional Neural Network layer shape.

Layer	Shape
Input	$140 \times 320 \times 1$
Conv2d	$136 \times 316 \times 16$
Pool2d	$34 \times 79 \times 16$
Conv2d	$30 \times 75 \times 32$
Pool2d	$6 \times 15 \times 32$
Dense	$2880 \times 1 \times 1$
Dense	$256 \times 1 \times 1$
Dense	$64 \times 1 \times 1$
Output	$1 \times 1 \times 1$

Table 6
CNN training performance.

	Loss	R^2 score	Samples
Train	$5.66 \cdot 10^{-4}$	0.9822	620
Validation	$9.53 \cdot 10^{-4}$	0.9670	133
Test	$9.17 \cdot 10^{-4}$	0.9758	133

Table 7
K-fold cross validation for CNN.

R^2 score	k = 1	k = 2	k = 3	k = 4	k = 5
Train	0.9776	0.9671	0.9830	0.9772	0.9762
Validation	0.9740	0.9702	0.9709	0.9771	0.9731
Test	0.9726	0.9725	0.9702	0.9757	0.9733

produce a 1D array that is processed by the dense layers to obtain the vane efficiency η_v value, represented by a single scalar value. The output value is normalized to compute the loss, then restored to its original value. The dataset includes 886 images divided in batches, with a size of 64. Leaky ReLU activation function is used in all the layers, except the last one where a linear activation is used.

The loss is computed with normalized target value, using the MSE criterion, the ADAM optimizer, and a fixed learning rate of 10^{-5}. L2 regularization with a weight decay of 10^{-6} is set and a dropout of 4% is applied to the first two dense layers to prevent overfitting. The training phase consisted in 2000 epochs, for a computational time of 1h 20m on 48 CPU cores. The results of the training phase are reported in Table 6. The Loss function reached a sufficiently low value while the accuracy reached a value over 96% for all the database's splits. The last trend is confirmed by the parity plots on Fig. 9, where almost all the points are close to the main diagonal, where the points presents the same value for the expected output and the prediction.

Cross-validation 5 fold was applied to the original train and validation dataset (85% of total cases), so the reduced dataset is trained on 4 of this fold and validated on 1, generating 5 different CNN configurations. The results are reported in Table 7. Each of the five different divisions reaches at least the 96% of the R^2 score, assessing that the model is insensitive to the division chosen for the training phase.

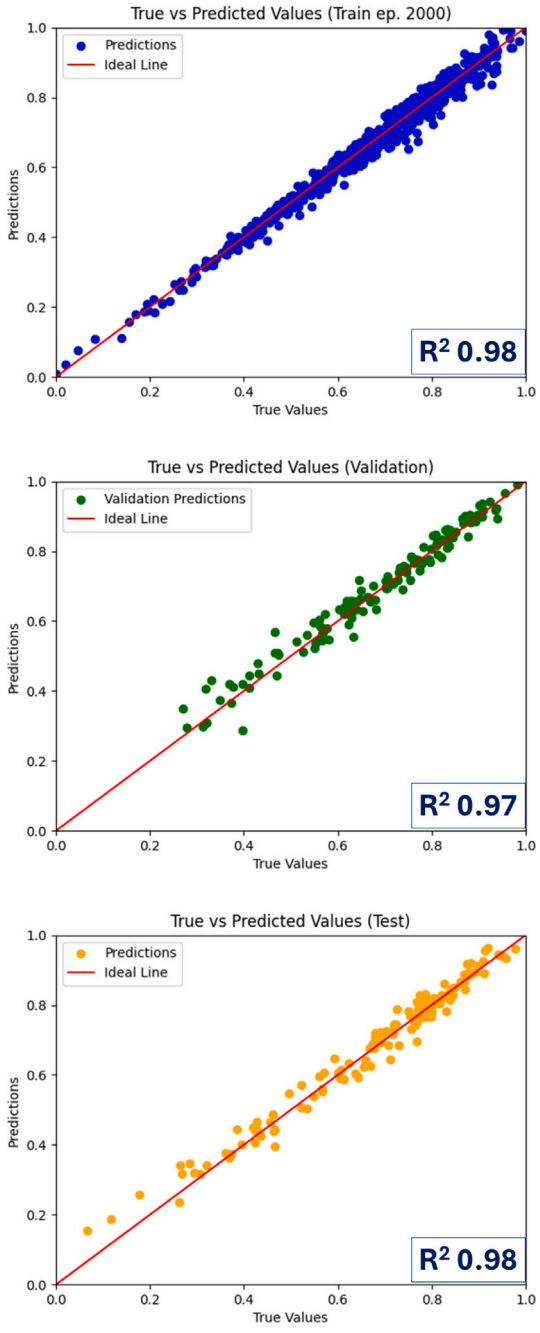

Fig. 9. CNN train, validation, test parity plots.

5.3. Optimization algorithm

Two different optimization algorithms are applied: the first one is Genetic algorithm, the second is Particle Swarm Optimization. The goal of the optimization process is to maximize the vane efficiency η_v. Both the algorithms generate a population of candidates that corresponds to an array of 18 values representing the control points to generate the profile, the endwalls and the stagger angle. These values are used to generate images that are fed into the fitness function that is the trained Convolutional Neural Network.

The Genetic algorithm is employed through the library *Numpy*, the main feature of the algorithm are reported in Fig. 10. Differently to what was done in the article of Nastasi et al. [18], two new feature are employed in the optimization algorithm to improve the research for

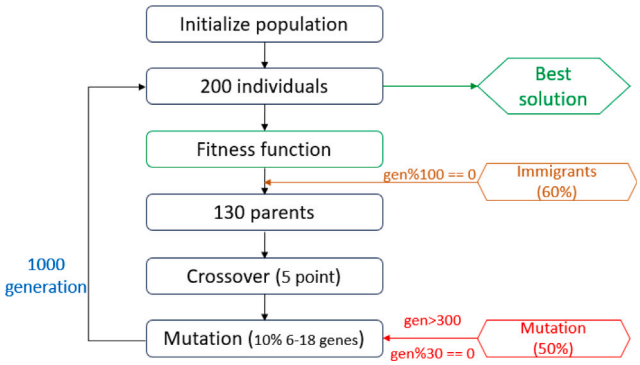

Fig. 10. GA flow chart.

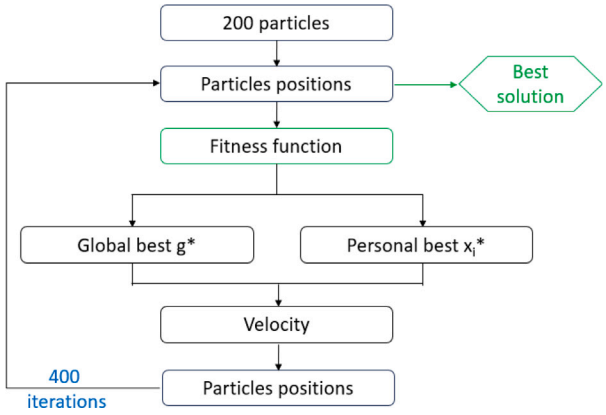

Fig. 11. PSO flow chart.

Table 8
Optimization algorithm predictions and CFD results.

Algorithm	$\eta_{v,CNN}$ [−]	$\eta_{v,CFD}$ [−]	Error	Ma_{in} [−]	α_2 [°]
GA	0.9193	0.9096	≈1%	0.52	73.23
PSO	0.9193	0.9101	≈1%	0.56	72.33

the best solution. After the first 300 generations, every 30 generation the mutation rate is increased from 10% to 50%, furthermore every 100 generations the 60% of the population is replaced with new individuals, this feature is referred as immigration in the literature. GA produced an optimal solution with $\eta_v = 0.9193$ after 1000 generations, it took 3 h 40 min on 48 cores.

The Particle Swarm optimization is also employed through the "Numpy" library, the main feature of the algorithm are reported in Fig. 11. The latter methods presented a faster convergence respect to former optimization method, it required 400 iterations (approximately 1 h 40 min) to find the optimal solution with $\eta_v = 0.9193$.

In Fig. 12, the endwall and the blade profile obtained with GA, PSO and the one from Nastasi et al. [18] are reported to have a visual comparison with the original baseline geometry. From now on the blade optimized with PSO is referred as CPSO, the one through GA as CGA and the blade of Nastasi et al. [18] as NGA.

The new blade and endwalls configurations generated by the optimization algorithms were tested using CFD RANS simulations, to understand the reliability of the trained CNN model. The results of the CFD analysis are summarized in Table 8: both configuration shows a vane efficiency $\eta_{v,CFD}$ of 0.91 and a relative error of approximately 1%. The CPSO blade achieved an high inlet Mach number respect to the CGA, furthermore the CGA blade presents an higher flow yaw angle. In Fig. 13 the Mach number for CPSO and CGA is represented as contour plot, it is interesting to notice the local acceleration that produces a thickening of the boundary layer in the proximity of the change of curvature in the suction side, which is more evident for the CPSO blade.

5.4. Unsteady analysis under pulsating boundary conditions

The optimized profiles and vanes obtained through the Genetic algorithm and the Particle Swarm Optimization are tested with pulsating boundary condition obtained from a Rotating Detonation Combustor and compared with the ones given by the Neural Network. The URANS analysis are initialized with the correspondent RANS data that correspond to the initial time step of the period. For each configuration, a total of 10 periods are simulated, ensuring cross-correlation values above 0.95 for the three variables of interest, as it is possible to see in Fig. 14.

Three configurations are analyzed according to the aforementioned performance parameters, and the results are available in Table 9. The weighted pressure mixed efficiency presented similar values for all the configurations, while the deviation coefficient and total pressure losses

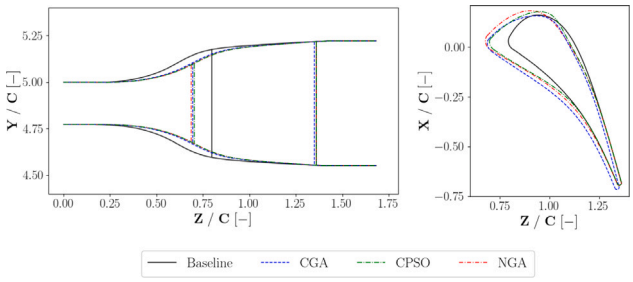

Fig. 12. Comparison of the blades optimized with different networks and algorithms.

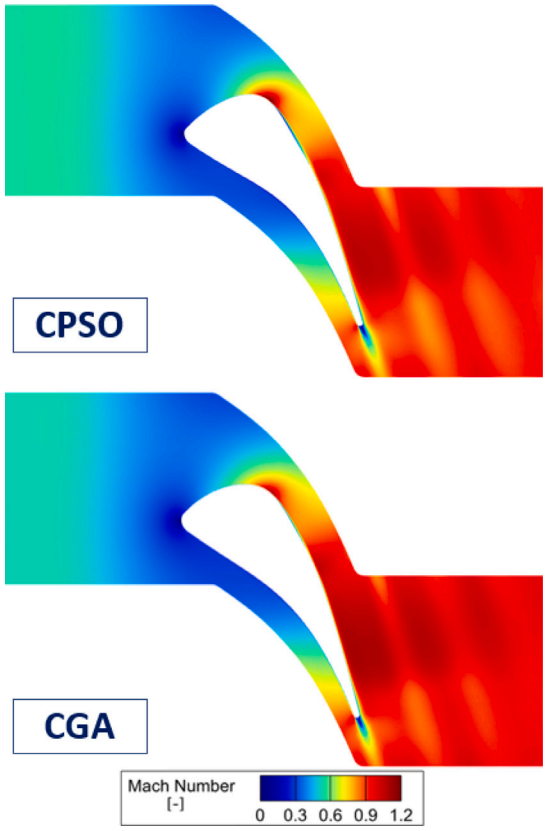

Fig. 13. Mach number contour plots for CGA and CPSO vane, evaluated through RANS simulations.

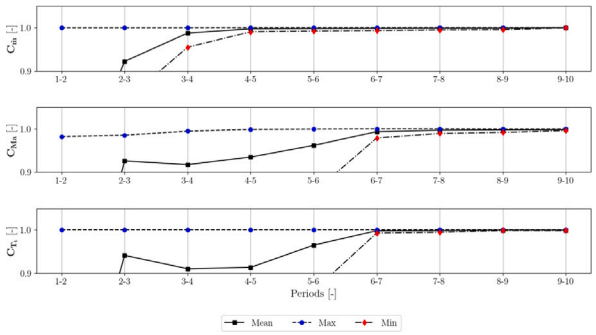

Fig. 14. Cross-correlation values for mass-flow rate, mach number, and total temperature, computed by means of a URANS CFD analysis.

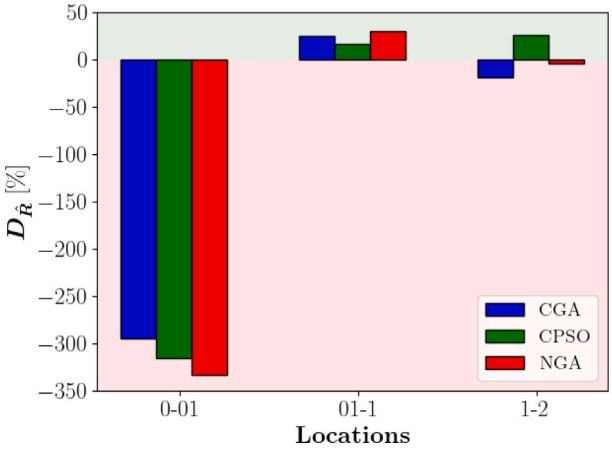

Fig. 15. Damping coefficients at different location of the domain.

Table 9
Performance parameters for evaluating the vane under pulsating boundary conditions.

	$(\overline{\eta_t})^{CA}$ [−]	$(\overline{\zeta_{Pt}})^{CA}$ [%]	$(\overline{\zeta_\alpha})^{CA}$ [%]	$D_{\hat{R}}$ [%]
NGA	0.898	5.66	1.41	−4.49
CGA	0.895	5.91	1.33	−19.40
CPSO	0.893	6.05	1.32	25.70

represented an opposite trend for the NGA and CPSO configurations. The damping coefficient of the pressure is computed in the locations identified in Fig. 2, which are the inlet of the domain, the inlet of the vane, the leading edge and the outlet section. The results of the analysis are reported in Fig. 15 and in Table 9 for the locations 1–2. The results stated that only the CPSO configuration produces an attenuation of the pressure signal from the inlet to the outlet of the vane, while the NGA and CGA configurations gave an enhancement.

In Fig. 16, normalized helicity contour plots for the optimized CPSO and CGA configurations are analyzed, according to 5 different time steps to highlight the behavior of secondary flows. Helicity is the dot product between vorticity and velocity and is mainly used to determine whether the vorticity vector is aligned with the flow field or not. Only the values beyond a certain threshold are shown in the contour plots to highlight the hub and casing vortices.

Due to the presence of diverging endwalls, negative pressure gradients are generated close to the vane leading edge, thus thickening the incoming boundary layer and increasing the inlet vorticity level with respect to conventional, straight channels. For that reason, the vorticity redistribution term in the vorticity equation [37] has a prominent role in the development of the secondary flows in the nozzle. Also, the pulsating nature of the inlet boundary condition greatly impacts the

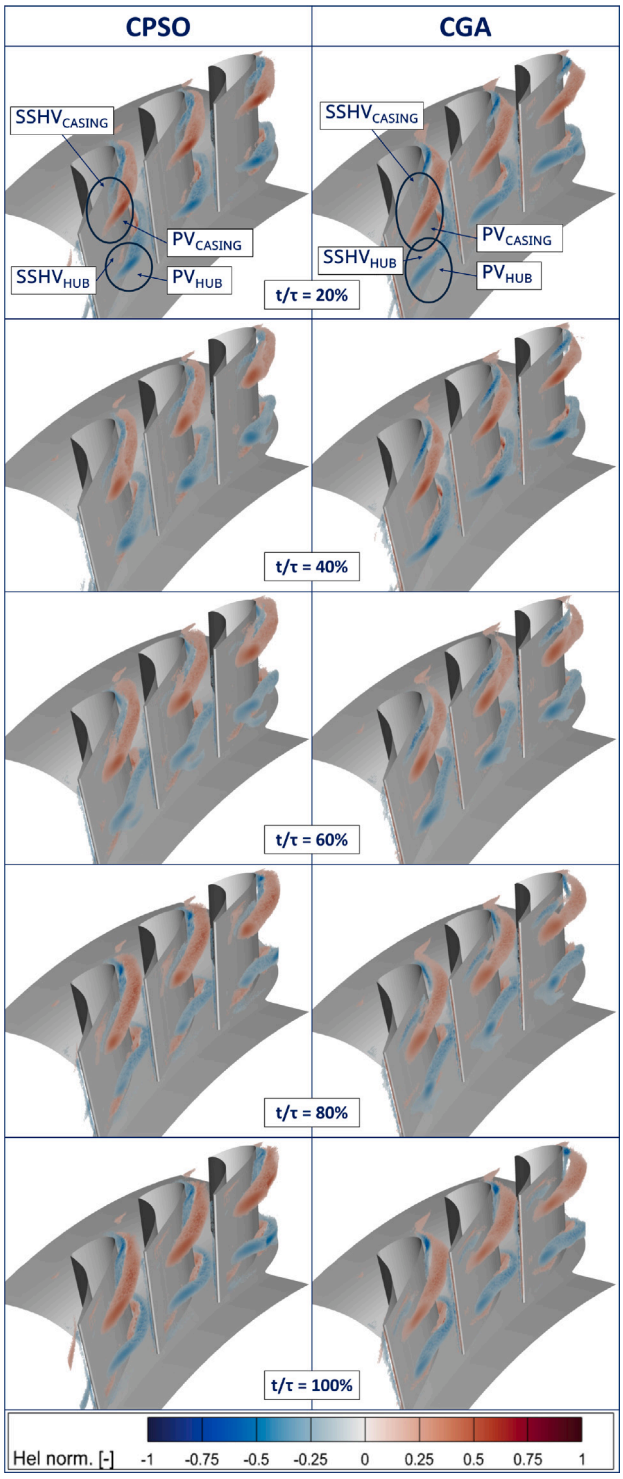

Fig. 16. Helicity contours for URANS simulations of the optimized blades in five different time steps, to highlight the intensity of secondary flows.

time-dependent development of secondary flows. For those reasons, it is hard to categorize the obtained secondary flows using the typical classification by Langston [38].

Nevertheless, observing the time steps reported in Fig. 16 two pairs of counter-rotating vortices can be individuated close to the vane hub and casing. The vortices characterized either by a positive normalized helicity value close to the casing or a negative value close to the hub demarcate the development of the Passage Vortex (PV) in the channel.

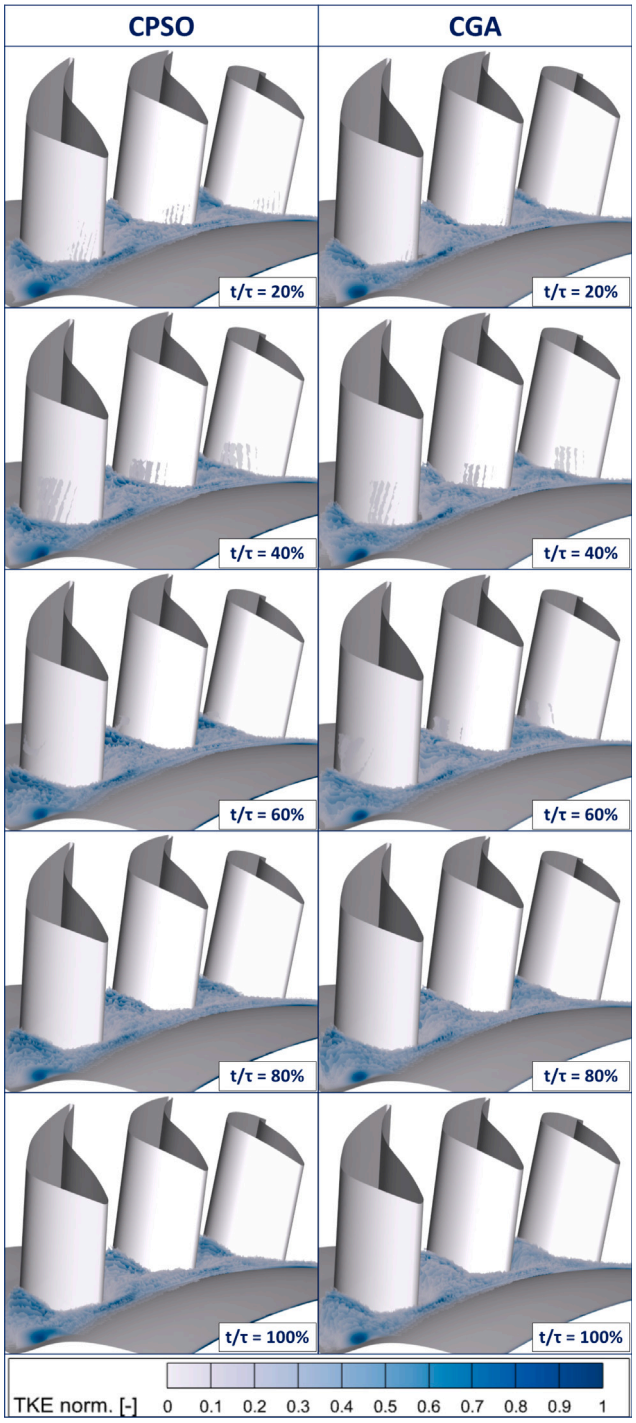

Fig. 17. Turbulent kinetic energy contours for URANS simulations of the optimized blades in different time steps, to highlight the magnitude of diffusive bubbles.

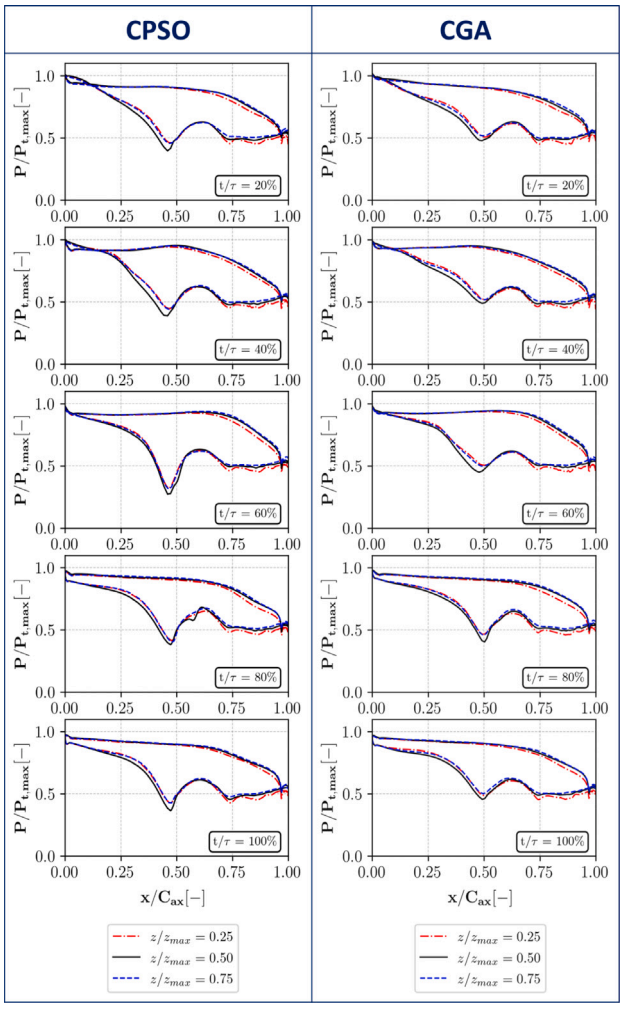

Fig. 18. Pressure distribution on blade surface for URANS simulations of the two optimized profiles, for five different time steps at three span heights.

On the contrary, the vortices with opposite signs mark the presence of the Suction Side leg of the Horseshoe Vortex (SSHV). The absence of a pressure side leg of the horseshoe vortex is a notable difference with respect to conventional HPT vane flows development (see for example Salvadori et al. [1]), probably caused by a early fusion with the PV (which usually inside of the nozzle).

Looking at the obtained results corresponding to the 20% of the period, for the CPSO vane the two pairs of secondary flows are positioned closer to the suction side in the azimuthal direction and more restricted to the casing in radial direction with respect to the CGA vane case. This trend is essentially confirmed for almost all time-steps, and it can justify the enhancement in the outlet total pressure signal for the CGA vane and for the attenuation for the CPSO vane.

Fig. 17 gives some insights about the leading edge region for both the vanes. The contour shows the turbulent kinetic energy of the structures in the hub region of both the vanes. Diffusive bubbles are present in both configuration, they can be noticed looking at the dark blue spot in the bottom left corner of every image. Suction side separation, due to the change of attack can be seen looking at the light violet strips at 20% and 40% of the period. The core of the diffusive bubble for the CPSO vane seems to move more in the axial direction respect to the CGA vane. This can explain the worse performance in damping coefficient for the CPSO respect to the CGA regarding the inlet of the domain-inlet of the vane region.

In Fig. 18, a comparison of CPSO and CGA blade loading for different time steps and span heights is reported. The pressure ratio is normalized by the maximum inlet total pressure reached during the pulsation period, to represent the same normalization for all the time steps. The region along the axial chord between 0 and 0.2 presents a shift of the stagnation point from the suction side to the pressure side, taking a look from time steps 20% to time steps 100%. This phenomenon is particularly evident on the CPSO blade where the suction side pressure is higher than the pressure side one in the time

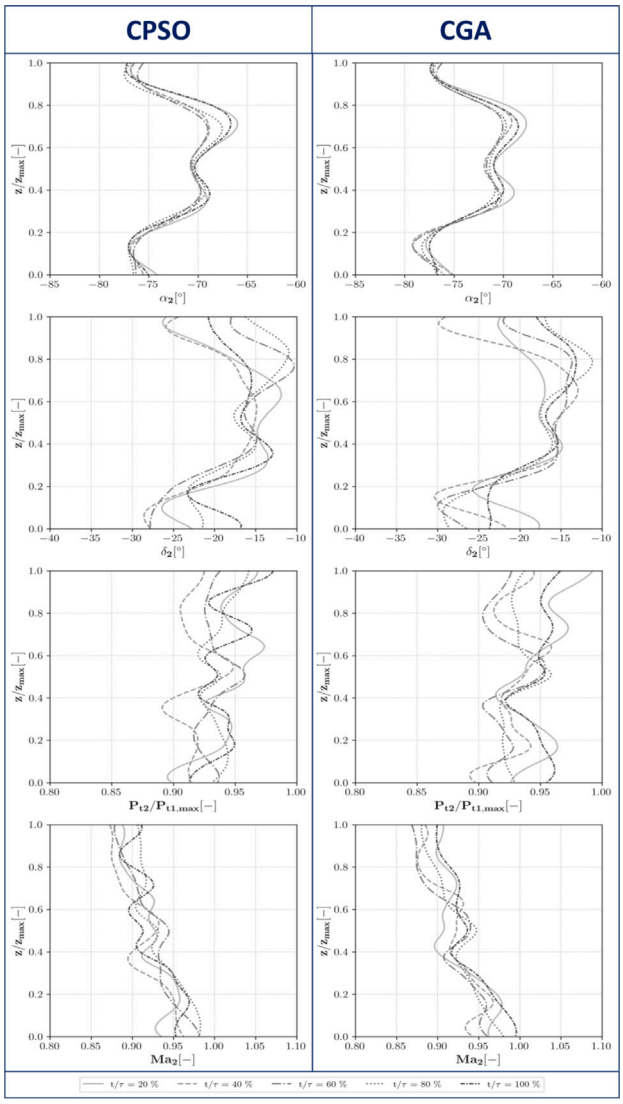

Fig. 19. Outlet radial averaged properties of yaw angle, pitch angle, total pressure, and Mach number for five different time steps of URANS simulations.

step 20%. The strong variation of the inlet yaw angle is responsible for this behavior.

The region of the blade up to $x/C_{ax} \approx 0.5$ is characterized by a curvature (of both blades) that produces a local acceleration, demonstrated by the pressure drop on the suction side. Flow acceleration for the CPSO blade is higher than the one of the CGA blade at all the blade heights. The flow decelerates between $x/C_{ax} \approx 0.5$ and 0.6, with a visible corresponding pressure rise. Again, this phenomenon is stronger in the CPSO blade, especially along time steps where the intensity of the pressure drop changes significantly.

The outlet region for CPSO e CGA configurations is analyzed in Fig. 19, by means of tangentially-averaged distributions of yaw angle, pitch angle, normalized total pressure and mach number. Yaw angle α_2 fluctuations along the span of both blades presents a similar trend as expressed by the deviation coefficient reported in Table 9, except for the mean value which is due to a different metal angle as stated in Table 8. The pitch angle δ_2 presents slightly larger fluctuations in the endwalls for CGA blade, the same trend is confirmed by the total pressure. This might explain the enhancement of the damping factor for the CGA blade as stated in Table 8. The outlet Mach Ma_2 number distribution presents a similar trend for both configurations.

Summarizing, CPSO and CGA configurations presents similar trends regarding the cycle average stator efficiency, the exit angle and pressure losses, as showed in Table 9. The pressure outlet signal is attenuated in the CPSO blade, which is enhanced in the CGA, for this reason the CPSO blade represents the more suitable configuration to ingest the synthetic boundary conditions.

6. Conclusions

The activity focused on the optimization of a HPT vane and diffusive endwall profiles with the goal to ingest a RDC flow at Ma $\simeq$ 0.6. The vane and endwall were parameterized using splines and modified by changing the position of the control points. The design space was explored through the LHS technique, for a total of 885 configurations that were analyzed with RANS CFD calculation.

CNN were trained in order to predict the vane efficiency for a given design point, directly relying on a black and white the image of the endwall and the vane. The CNN proved to be an efficient and reliable tool to estimate the vane efficiency, giving an R^2 score over 0.96 for validation and test. Two different nature-inspired algorithms were implemented to train the CNN and find the parameters that maximizes the vane efficiency. Both methods gave the same results in term of vane efficiency with different geometrical parameters.

The two optimized configuration and the one optimized through a DNN are studied by means of a URANS analysis, imposing realistic RDC outlet boundary conditions that reproduce oscillations in total pressure, total temperature and inlet flow angle. The three configurations provided similar results in terms of cycle average efficiency, loss deviation coefficient, and total pressure losses, but only the CPSO blade and endwall provided an attenuation of the total pressure signal in the outlet of the vane, proving to be the most suitable configuration to face a RDC outlet flow field.

Future works could focus on extending this optimization strategy to either different vane profiles or different combustor outlet conditions, including the new inlet boundary conditions in the DOE phase, allowing to the CNN architecture to be more general.

CRediT authorship contribution statement

Giovanni Labrini: Writing – review & editing, Writing – original draft, Visualization, Validation, Software, Methodology, Investigation, Formal analysis, Data curation, Conceptualization. **Rosario Nastasi:** Visualization, Validation, Software, Methodology, Investigation, Formal analysis, Conceptualization. **Simone Salvadori:** Writing – review & editing, Validation, Supervision, Resources, Project administration, Investigation, Funding acquisition, Conceptualization. **Daniela Anna Misul:** Writing – review & editing, Validation, Supervision, Resources, Project administration, Methodology, Funding acquisition, Conceptualization.

Declaration of competing interest

The authors declare the following financial interests/personal relationships which may be considered as potential competing interests: Simone Salvadori reports financial support was provided by European Union - Next Generation EU, in the frame of the "Enabling Technologies for Turbine Design in CO2-Free Rotating Detonation Engines (EnaTech-RDE)", Mission 4, Component 1, CUP E53D23003110001.

Acknowledgments

The authors are grateful to Panagiotis Gallis for sharing the original database of geometries and for his support in the definition of the numerical analysis. The authors acknowledge the CINECA award under the Iscra-C initiative for the permission tu use the GALILEO100 cluster under the RDE-FC project (HP10CZYJU7). The authors acknowledge

HPC@POLITO for the availability of high-performance computing resources and for the support. The authors acknowledge the TATEF2 consortium (EU-funded project under FP6, contract AST3-CT-2004-502924) for the permission to use the data generated at the von Karman Institute for Fluid Dynamics. Both the Italian Ministry of Education, Universities and Research and the European Commission are acknowledged for the support provided to the "Enabling Technologies for Turbine Design in CO2-Free Rotating Detonation Engines (EnaTech-RDE)" project (CUP E53D23003110001) funded through the PRIN 2022 call financed by the Next Generation EU action.

Data availability

Data will be made available on request.

References

[1] Salvadori S, Insinna M, Martelli F. Unsteady flows and component interaction in turbomachinery. Int J Turbomach Propuls Power 2024;9(2):15. http://dx.doi.org/10.3390/ijtpp9020015.
[2] Perkins H, Paxson D. Summary of pressure gain combustion research at NASA. Technical Report, NASA/TM-2018-219874, 2018.
[3] Glassman I, Yetter R, Glumac N. Flame phenomena in premixed combustible gases. In: Combustion. 5th ed.. Waltham: Academic Press; 2015.
[4] Hishida M, Fujiwara T, Wolanski P. Fundamentals of rotating detonations. Shock Waves 2009.
[5] Lu F, Braun E. Rotating detonation wave propulsion: Experimental challenges, modeling, and engine concepts. J Propuls Power 2014.
[6] Sousa J, Paniagua G, Collado Morata E. Thermodynamic analysis of a gas turbine engine with a rotating detonation combustor. Appl Energy 2017;195:247–56. http://dx.doi.org/10.1016/j.apenergy.2017.03.017.
[7] Schwer D, Kailasanath K. Numerical investigation of rotating detonation engines. In: 46th AIAA/ASME/SAE/ASEE joint propulsion conference & exhibit. Nashville, TN: American Institute of Aeronautics and Astronautics; 2010, p. 2195–202. http://dx.doi.org/10.2514/6.2010-6880.
[8] Schwer DA, Brophy CM, Kelso RH. Pressure characteristics of an aerospike nozzle in a rotating detonation engine. In: 2018 joint propulsion conference. Cincinnati, OH: American Institute of Aeronautics and Astronautics; 2018, p. 4968. http://dx.doi.org/10.2514/6.2018-4968.
[9] Liu Z, Braun J, Paniagua G. Integration of a transonic high-pressure turbine with a rotating detonation combustor and a diffuser. Int J Turbo Jet Engines 2023;40:1–10.
[10] Liu Z, Braun J, Paniagua G. Performance of axial turbines exposed to large fluctuations. In: 53rd AIAA/SAE/ASEE joint propulsion conference. Atlanta, GA: American Institute of Aeronautics and Astronautics; 2017, p. 4817. http://dx.doi.org/10.2514/6.2017-4817.
[11] Grasa S, Paniagua G. Design, multi-point optimization and analysis of diffusive stator vanes to enable turbine integration into rotating detonation engines. ASME J Turbomach 2024;146(11):111002. http://dx.doi.org/10.1115/1.4065436.
[12] Gallis P, Salvadori S, Misul DA. Numerical analysis of a flow control system for high-pressure turbine vanes subject to highly oscillating inflow conditions. J Turbomach 2025;147:121008. http://dx.doi.org/10.1115/1.4068877.
[13] Queipo NV, Haftka RT, Shyy W, Goel T, Vaidyanathan R, Tucker PK. Surrogate-based analysis and optimization. Prog Aerosp Sci 2005;41:1–28. http://dx.doi.org/10.1016/j.paerosci.2005.02.001.
[14] Rai MM, Madavan NK. Aerodynamic design using neural networks. AIAA J 2000;38:173–82. http://dx.doi.org/10.2514/2.953.
[15] Renganathan SA, Maulik R, Ahuja J. Enhanced data efficiency using deep neural networks and Gaussian processes for aerodynamic design optimization. Aerosp Sci Technol 2021;111:106522. http://dx.doi.org/10.1016/j.ast.2021.106522.
[16] Li J, Cai J, Qu K. Surrogate-based aerodynamic shape optimization with the active subspace method. Struct Multidiscip Optim 2018;59:403–19. http://dx.doi.org/10.1007/s00158-018-2069-6.
[17] Du Q, Li Y, Yang L, Liu T, Zhang D, Xie Y. Performance prediction and design optimization of turbine blade profile with deep learning method. Energy 2022;254:124351. http://dx.doi.org/10.1016/j.energy.2022.124351.
[18] Nastasi R, Labrini G, Salvadori S, Misul DA. Shape optimization of a diffusive high-pressure turbine vane using machine learning tools. Energies 2024;19961073:17–22. http://dx.doi.org/10.3390/en17225642.
[19] Sieverding CH, Arts T, Dénos R, Martelli F. Investigation of the flow field downstream of a turbine trailing edge cooled nozzle guide vane. ASME Pap 1994;13. http://dx.doi.org/10.1115/94-GT-209.
[20] Dénos R, Sieverding CH, Michelassi V. Experimental investigation of the unsteady rotor aerodynamics of a transonic turbine stage. Proc Inst Mech Eng A 1999;213(4). http://dx.doi.org/10.1243/0957650991537653.
[21] Dénos R, Arts T, Paniagua G, Michelassi V, Martelli F. Investigation of the unsteady rotor aerodynamics in a transonic turbine stage. J Turbomach 2001;123(1):81–9.
[22] Paniagua G, Dénos R, Almeida S. Effect of the hub endwall cavity flow on the flow-field of a transonic high-pressure turbine. J Turbomach 2004;126(4):578–86.
[23] Liu Z, Braun J, Paniagua G. Three dimensional optimization for subsonic axial turbines operating at high unsteady inlet Mach number. In: 2018 joint propulsion conference. 2018, p. 4480.
[24] Cumpsty N, Horlock J. Averaging nonuniform flow for a purpose. ASME J Turbomach 2006;19961073:120–9. http://dx.doi.org/10.1115/1.2098807.
[25] George A, Driscoll R, Gutmark E, Munday D. Experimental comparison of axial turbine performance under steady and pulsating flows. ASME J Turbomach 2014;136(11):111005. http://dx.doi.org/10.1115/1.4028115.
[26] Xisto C, Petit O, Grönstedt T, Rolt A, Lundbladh A, Paniagua G. The efficiency of a pulsed detonation combustor–axial turbine integration. Aerosp Sci Technol 2014;82–83:80–91. http://dx.doi.org/10.1016/j.ast.2018.08.038.
[27] Suresh A, Hofer DC, Tangirala VE. Turbine efficiency for unsteady, periodic flows. J Turbomach 2012;134(3):034501. http://dx.doi.org/10.1115/1.4003246.
[28] Young JB, Horlock JH. Defining the efficiency of a cooled turbine. J Turbomach 2006;128(4):658–67. http://dx.doi.org/10.1115/1.2218890.
[29] Ornano F, Braun J, Saracoglu BH, Paniagua G. Multi-stage nozzle-shape optimization for pulsed hydrogen–air detonation combustor. Adv Mech Eng 2017;9(2):1687814017690955.
[30] Braun J, Paniagua G, Falempin F, Le Naour B. Design and experimental assessment of bladeless turbines for axial inlet supersonic flows. J Eng Gas Turbines Power 2020;142(4):041024.
[31] Uhl G, Taileb S, Zurbach S, Odier N, Poinsot T, Bellenoue M. Phenomenological aerodynamic analysis of an ejector exposed to large inlet pulsations. J Propuls Power 2025;41(2):178–89.
[32] Zhang A, Lipton ZC, Li M, Smola AJ. Dive into deep learning. Cambridge University Press; 2023, https://D2L.ai.
[33] Kingma DP, Ba J. Adam: A method for stochastic optimization. In: 3rd international conference for learning representations. 2015, http://dx.doi.org/10.48550/arXiv.1412.6980.
[34] Holland J. Adaptation in natural and artificial systems: An introductory analysis with applications to biology, control, and artificial intelligence. The MIT Press; 1992.
[35] Kennedy J, Eberhart R. Particle swarm optimization. In: Proceedings of ICNN'95-international conference on neural networks. Vol. 4, ieee; 1995, p. 1942–8. http://dx.doi.org/10.1109/ICNN.1995.488968.
[36] Yang X-S. Nature-inspired optimization algorithms. Elsevier; 2014.
[37] Lakshminarayana B. Fluid dynamics and heat transfer of turbomachinery. Wiley; 1995, http://dx.doi.org/10.5860/choice.33-5735.
[38] Langston L. Secondary flows in axial turbines-a review. Ann New York Acad Sci 2006;934(1):11–26.